RESEARCH ARTICLE | SEPTEMBER 06 2024

Margination behavior of a circulating cell in a tortuous microvessel

Ali Kazempour ; Peter Balogh

Physics of Fluids 36, 091907 (2024)
https://doi.org/10.1063/5.0227716
CHORUS

Physics of Fluids ARTICLE pubs.aip.org/aip/pof

Margination behavior of a circulating cell in a tortuous microvessel

Cite as: Phys. Fluids **36**, 091907 (2024); doi: 10.1063/5.0227716
Submitted: 10 July 2024 · Accepted: 17 August 2024 ·
Published Online: 6 September 2024

View Online Export Citation CrossMark

Ali Kazempour and Peter Balogh[a)]

AFFILIATIONS

Department of Mechanical and Industrial Engineering, New Jersey Institute of Technology, Newark, New Jersey 07114, USA

[a)]Author to whom correspondence should be addressed: peter.balogh@njit.edu

ABSTRACT

In the mammalian microcirculation, circulating cells (CCs) such as white blood cells or cancer cells can be forced to flow alongside the vessel wall through hydrodynamic interactions with red blood cells (RBCs). This phenomenon, known as margination, plays an important role in physiology as it precedes the extravasation of a CC from the bloodstream into surrounding tissue. Current knowledge of the fluid mechanics influencing margination is primarily based on idealized straight tube flow. Microvessels *in vivo*, however, are often observed to be tortuous, and the influence of this morphology on CC margination is largely unknown. In the current work, we utilize high-fidelity three-dimensional (3D) cell-resolved simulations to study the margination behavior of a CC flowing with RBCs through a tortuous microvessel over a range of conditions typical of the microcirculation. We observe cross-stream lateral CC movement in response to local curvature, which generally augments the ability of the CC to reach the near-wall region. Once the CC marginates, the presence of RBCs in the central region tends to lock the CC in the near-wall cell-free layer. The overall impact of tortuosity on the degree of margination, however, is mixed. At low hematocrit, tortuosity provides a fluid dynamics-derived mechanism to grant CCs access to near-wall locations under conditions where this behavior generally does not occur in a straight tube. At higher hematocrit where a CC can easily marginate in a straight tube, the varying local curvature causes intermittent motion away from the wall thus slightly reducing the degree of margination.

I. INTRODUCTION

The transport of circulating cells (CCs) through the blood microcirculation plays a central role in various physiological and pathophysiological processes in our bodies.[1] Common examples of CCs include leukocytes (white blood cells, or WBCs), which provide the body's defense against infection or circulating tumor cells (CTCs) that facilitate metastatic spread of cancer.[2,3] CCs typically flow *in vivo* with red blood cells (RBCs), the primary cellular constitute of blood, and hydrodynamic interactions give rise to a phenomenon known as margination where the CC is induced to flow alongside the vessel wall.[2,4,5] RBCs, being greater in number and more deformable than a CC, tend to occupy the central vessel region[6–8] and laterally displace the CC to the margins of the vessel. The importance and physiological relevance of margination lies in its potential to provide a pathway for CC adhesion to the endothelium, ultimately leading to extravasation into surrounding tissue (e.g., site of infection for a WBC, or distant organ for a CTC). Works have reported CC margination and adhesion to be most pronounced in the venular part of the microcirculation.[2,9,10] While tortuous microvessels have been observed in both the arterial and venular microcirculation,[11–14] the prevalence of CC margination in the latter highlights a potential role played by this morphology therein. To date, however, computational studies involving CC margination have primarily considered straight tubes and channels.[15–18] Effects of vessel tortuosity on the coupled interaction between RBCs and a CC are thus largely unknown, and new studies are needed to advance current understanding of margination as it likely occurs *in vivo*.

The fluid dynamics of flows in curved vessels have distinct differences from flows in straight tubes. Notable among these differences is that at the low Reynolds numbers typical of the microcirculation[19] ($\mathrm{Re} \ll 1$), the cross-sectional velocity profile is skewed in a curved vessel toward the side with higher curvature.[20–23] The location on the cross section of minimum local shear rate will thus also be shifted toward the higher curvature side, which contrasts from a straight tube where the location of minimum shear is at the vessel center. During transport through a vessel, a deformable cell will laterally migrate in the direction of decreasing shear rate,[24] and thus, in a straight tube, a single deformable cell will tend to flow near the vessel centerline. In a curved tube, however, recent work has shown how at low Re a deformable cell will tend to flow closer to the side of the vessel with higher curvature,[25,26] demonstrating wall-directed movement in response to

the altered velocity profile. This behavior unique to a curved tube is particularly relevant to CC margination because it suggests a causal role played by vessel morphology. Furthermore, wall-directed CC movement in a curved vessel in the absence of RBCs marks a notable departure from straight tube behavior where RBCs are required to drive a CC toward the wall.

A common modeling paradigm for capturing CC transport behavior through the microcirculation is to consider a CC as a deformable cell that is spherical in shape, with the primary CC material property being its deformability.[3,15–18,27,28] Many studies focused on CC margination behavior and dependencies on hemodynamic conditions have considered WBCs,[15,16,18,27] while others have considered CTCs.[3] Works have also used this cell model to study CTC adhesion, including isolated CTCs without RBCs in tubes[29] as well as with RBCs in a vessel network.[30] Furthermore, this model was demonstrated to yield good agreement with experiments capturing cell transport through small passages that could distinguish between cancer cell types.[31] Such a model naturally neglects many micro and nano-scale complexities unique to WBCs or CTCs,[32,33] but in terms of transport through the blood microcirculation, the above works have established the ability of this CC representation to accurately capture the transport behavior in question. Furthermore, such works have demonstrated that a CC modeled in this manner effectively serves as a proxy for either a WBC or a CTC when considering microcirculatory transport behavior.

Experimental observations of CC margination in the blood microcirculation *in vivo*[2,10] have been aided by the existence of a near-wall region devoid of RBCs,[34,35] often referred to as the cell-free layer (CFL). For a suspension of deformable RBCs, both lateral lift forces[6,7,24,36,37] and cell–cell interactions[38,39] (i.e., shear-induced diffusion) compete, generally resulting in an RBC-rich central core region and the near-wall CFL as shown by experimental and computational works spanning decades.[25,40–45] In a straight tube, the CFL is axisymmetric but for complex vessel morphologies the CFL is 3D and asymmetric, as has been quantified recently for vessels in 3D microvascular networks[25] and tortuous microvessels.[46] The CFL is an important hemodynamic feature related to margination; as a CC migrates toward the wall, the CFL is where the CC surface first becomes exposed to the endothelium. A CC surface entering the CFL thus presents a favorable configuration to permit adhesion to the endothelium. The thickness of the CFL *in vivo* is highly heterogenous, due to both vessel geometry as well as hemodynamic conditions, and has been reported to range anywhere from approximately 0.5 to 5.0 μm.[40–44] Microvilli on the CC surface which facilitate adhesion to the endothelium have also been reported to range anywhere from 0.2 to 2 μm.[47–49] Prior works providing insights into the mechanisms driving margination in straight tubes have typically considered a fixed distance from the wall when identifying a marginated CC. Yet, this heterogeneity and overlap between CFL thicknesses and microvilli lengths suggest more detailed consideration of near-wall CC residence guided by 3D hemodynamics can improve mechanistic understanding of margination in tortuous microvessels. Furthermore, the complex 3D shape of the CFL due to vessel complexity and the varying hemodynamic conditions typical of the microcirculation highlight the need for new studies that can capture intricate 3D details of the cell-resolved fluid dynamics.

Hemodynamic characteristics that have been shown to influence margination include the tube hematocrit (H_T) or RBC volume fraction[15,17,50] and the flow strength[2,15,16,51] often quantified in terms of the effective shear rate ($\dot{\gamma}_{eff}$). While the means by which H_T and $\dot{\gamma}_{eff}$ influence margination is complex, works have generally shown H_T levels in the 20%–30% range to be most favorable in addition to $\dot{\gamma}_{eff}$ values generally less than 100 s^{-1}. At lower H_T conditions, the RBC volume fraction is generally not sufficient to displace the CC toward the wall, while at higher H_T, the RBC-CC interactions can effectively pull the CC away from the wall.[15,50] Other factors such as RBC aggregation have been shown to enhance margination[2,9,17,51] relative to the above discussion, but works have demonstrated this feature is not necessary for margination.[15,16,50] The identification and quantification of these relationships between margination behavior and hemodynamic conditions have provided important insights to aid in understanding the mechanisms which influence margination. As mentioned, however, this current knowledge is based on RBC- and CC-resolved flows in straight tubes and channels. Work involving an isolated CC in the absence of RBCs flowing through an idealized curved tube demonstrated how curvature can have a significant influence on CC adhesion.[29] Yet, the role played by vessel morphology, and specifically tortuosity, in influencing *in vivo* CC transport with RBCs remains unclear.

Toward this end, in the current work, we use 3D cell-resolved simulations in a tortuous microvessel digitally reconstructed from *in vivo* images to provide new insights into the mechanisms which influence CC margination under such conditions. Data are first presented for CC transport without RBCs, demonstrating cross-stream lateral movement directly following the local vessel curvature. CC margination behavior with RBCs is subsequently analyzed and discussed. H_T levels of 10%, 20%, and 30% are considered as well as effective shear rates of 25, 50, and 100 s^{-1} in order to cover a range of conditions typical of the microcirculation. The high-resolution output data are used to define a margination plane adapted to local CC position and vessel shape, which facilitates quantification of and comparison between CC and RBC residence behavior across all cases. Complex 3D CFL characteristics are used to quantify CC residence in and across the CFL, providing a comprehensive picture of the near-wall behavior. Finally, behavior in the tortuous microvessel is compared to that in an equivalent straight tube, directly quantifying the impact of tortuosity on CC margination. Elucidating behavioral characteristics is important toward building a more complete understanding of the margination phenomena as it likely occurs *in vivo*.

II. METHODS

A. Cell-resolved simulations in complex geometry

Three-dimensional computational fluid dynamics simulations are performed using an immersed boundary method (IBM)-based approach to model biophysical flows in complex geometries. Salient details relevant to the current work are provided here, while full details of the method can be found in prior work[52] in addition to extensive validations against both experiments and analytical theory.[25,52–55] Reynolds numbers in the microcirculation are typically small[19] (i.e., $\ll 1$), and thus, we model the unsteady Stokes equations for a constant density (ρ), variable viscosity [$\mu(\boldsymbol{x}, t)$] fluid along with the conservation of mass for an incompressible fluid:[56]

$$\rho \frac{\partial \mathbf{u}}{\partial t} = -\nabla P + \nabla \cdot \left[\mu(\nabla \mathbf{u} + \nabla \mathbf{u}^T)\right] + F, \quad (1)$$

$$\nabla \cdot \mathbf{u} = 0, \quad (2)$$

where the body force term $\boldsymbol{F}$ comprises stresses in the deformable cell membranes, as discussed later. These governing equations are solved

on a fixed, uniform Eulerian grid using a finite volume/spectral method with a staggered-grid discretization of the velocity (**u**) and pressure (P) fields. Complex vessel boundaries (e.g., tortuous microvessel walls) are incorporated using a sharp-interface IBM, which augments the discretized governing equations at grid points immediately adjacent to the vessel walls (i.e., outside the fluid domain) to enforce a no-slip condition at the interface. The physical location of the interface as it extends through the computational domain is identified using a triangular mesh fit to the surface of a digitally reconstructed vessel.

Deformable cells (i.e., CC and RBCs) are modeled within this approach using a continuous forcing IBM. Each cell surface in its undeformed state is discretized by a triangular Lagrangian mesh which both deforms in response to fluid motion and imparts a local force field to the fluid in response to deformation. This two-way coupling is achieved by means of a delta function (δ), where the velocity at each Lagrangian mesh node ($\boldsymbol{U}$) is first interpolated from the Eulerian velocity field (**u**) as

$$\boldsymbol{U} = \int_V \mathbf{u}\delta(\boldsymbol{x} - \boldsymbol{X})\mathrm{d}V, \tag{3}$$

where $\boldsymbol{x}$ and $\boldsymbol{X}$ correspond to coordinates on the Eulerian and Lagrangian grids, respectively. $\boldsymbol{U}$ is subsequently integrated to move each Lagrangian node and deform the cell. The stress generated in each Lagrangian triangular element is determined using the finite element method (FEM), as described below. These elemental forces ($\boldsymbol{f}_e$) are transferred to Lagrangian nodes using box-spline shape functions, and the nodal forces ($\boldsymbol{f}_n$) are spread to the Eulerian grid using the same delta function as in Eq. (3),

$$F = \int_S \boldsymbol{f}_n\delta(\boldsymbol{x} - \boldsymbol{X})\mathrm{d}\boldsymbol{X}, \tag{4}$$

where $\boldsymbol{F}$ is the body force term in Eq. (1). The delta function in Eqs. (3) and (4) is evaluated by means of a cosine function with stencil spanning four Eulerian grid points in each of the x, y, and z directions.[52]

Experiments have shown that the hemoglobin comprising the interior of an RBC generally behaves as an incompressible Newtonian fluid with viscosity five times greater than the plasma with which RBCs flow.[57] Our model accounts for this variable viscosity field on the Eulerian grid whereby grid points internal to each RBC have an elevated viscosity compared to the plasma outside in accordance with this ratio. Eulerian grid points interior to all deformable cells are tracked by means of an indicator function $I(\boldsymbol{x}, t)$, which is zero outside a deformable cell and one inside a deformable cell. This function is used to define the 3D viscosity field on the Eulerian grid corresponding to an instantaneous RBC configuration:

$$\mu(\boldsymbol{x}, t) = \mu_p + (\mu_c - \mu_p)I(\boldsymbol{x}, t), \tag{5}$$

where μ_p is the plasma dynamic viscosity and μ_c is the viscosity of the cytoplasmic fluid (i.e., hemoglobin), whose physical values are approximately 1.2 and 6 cP, respectively.[58] Spatial derivatives of $\mu(\boldsymbol{x}, t)$ in Eq. (1) are evaluated using second-order differencing.

For the current work where we model RBCs and a CC, a separate indicator function is used for each cell type in order to individually track CC and RBC residence behavior for postprocessing and analysis. The indicator function is related to the cell surface normals (**n**) and delta function via a Poisson equation as[59]

$$\nabla^2 I = \nabla \cdot \left[\int_S \delta(\boldsymbol{x} - \boldsymbol{X})\mathbf{n}\, dS\right], \tag{6}$$

which we solve using a spectral approach as described elsewhere.[52]

B. Deformable cell models and physical characteristics

In the current work, we model a CC as a deformable cell that is spherical in shape and stiffer than an RBC. This representation follows experimental observations of CCs during transport through the microcirculation[2,3,10] and, as previously mentioned, has been extensively employed across modeling studies on CC margination and other transport behavior in the microcirculation. The same underlying cell model is employed for both the CC and RBCs, with the primary differences being their initial undeformed shapes and degree of deformability. Each RBC is modeled as an infinitesimally thin elastic membrane enclosing hemoglobin. The undeformed shape is a biconcave discocyte with a major axis of 7.8 μm, surface area of 134.1 μm^2, and volume of 94.1 μm^3 following experimental observations.[60] We consider a CC that is initially spherical in shape with a diameter of 10 μm, which is a representative size of such cells observed in the microcirculation.[2,3,10] CCs are typically 2–10 times stiffer than RBCs,[3,61] and to account for this difference, we consider the CC to have a capillary number ($Ca = \frac{\mu U_{ch}}{G_s}$) five times lower than each RBC. Here, μ is the plasma dynamic viscosity, U_{ch} is a characteristic velocity scale, and G_s is the membrane shear elastic modulus. For each RBC, we consider $G_s = 5 \times 10^{-6}$ N/m following that reported for healthy RBCs,[62] and for all simulations, we consider $Ca_{RBC} = 1$ and $Ca_{CC} = 0.2$. Similar to the RBCs, the interior of the CC is also modeled as a Newtonian fluid. For the CC, we consider an interior viscosity equal to that of the plasma with which it is conveyed, and thus the resistance to deformation is solely due to the membrane properties. Discussion on the justification for and implications of this modeling approach is provided in Sec. IV.

The membrane of each cell surface is discretized by a Lagrangian mesh of 5120 triangular elements, and each cell is modeled as resisting shear, area dilation, and bending. The membrane stress response to deformation is calculated using a Loop subdivision-based finite element method,[63,64] where the force density at each surface element is determined by evaluating the surface gradient of the Cauchy tension tensor (T^{mn}), membrane stress (σ^{mn}), and bending stress (ν^{mn}) as

$$\boldsymbol{f}_e = \nabla_s(T^{mn} + \sigma^{mn} + \nu^{mn}). \tag{7}$$

T^{mn} is calculated based on an energy function (W_s) developed for RBCs[65]

$$T^{mn} = \frac{2}{J_s}\frac{\partial W_s}{\partial I_1}A^{0mn} + 2J_s\frac{\partial W_s}{\partial I_2}A^{mn}, \tag{8}$$

where[62]

$$W_s = \frac{G_s}{4}\left[\left(I_1^2 + 2I_1 - 2I_2\right) + CI_2^2\right], \tag{9}$$

and I_1 and I_2 are the strain invariants, A is the metric tensor, G_s is the membrane shear elastic modulus previously mentioned, and C is a constant related to the area dilation modulus which we take to be 100.[52] The parameter C is purely a numerical parameter used to facilitate the constraint of constant surface area. Generally speaking, increasing the value of C decreases the degree to which the surface

area varies as the cell deforms, but at the expense of numerical stability. We use a value of 100 because we observe this to result in surface area changes <0.1% and stable simulations. Regarding conserving cell volume, we note that no extra force is utilized. Through monitoring of the volume change of each deformable cell, the maximum was calculated to be less than 0.2% on average for the current simulations, and thus, no extra force was used. σ^{mn} and ν^{mn} are calculated from the Helfrich bending energy as[64]

$$\sigma^{mn} = \frac{k_b}{2}(4\kappa^2 A^{mn} - 8\kappa B^{mn}), \tag{10}$$

$$\nu^{mn} = \frac{k_b}{2}(4\kappa A^{mn}), \tag{11}$$

where k_b is the bending modulus, κ is the mean curvature, and B is the curvature tensor.

In order to prevent the deformable cell membranes from overlapping the vessel walls, a short-range repulsive force (i.e., lubrication-type force) is utilized at the Lagrangian nodes for each cell with magnitude varying as the inverse distance cubed. Regarding potential overlap between deformable cell membranes, no additional measures are utilized; the force at each Lagrangian node is spread onto the Eulerian grid a small finite distance around each node, and we observe this to act like a lubrication layer preventing overlap. Such conditions have been rigorously tested in the development and validation of the method[52,66] as well as subsequent studies,[46,53,67] which monitor for overlap during all simulations.

C. Description of simulations and cases considered

An overview of the CC transport simulations is provided in Fig. 1. A simulation snapshot for a representative case is shown in Fig. 1(a), depicting the CC flowing with RBCs along with a zoomed-in view of the CC during transport [Fig. 1(c)]. The *in vivo* image of the rat mesentery from which the microvessel was digitally reconstructed is shown in Fig. 1(b). The undeformed RBC and CC shapes are given in Fig. 1(d). RBC-resolved simulations in this tortuous microvessel were described in our recent work[46] which focused on elucidating hemodynamic characteristics (e.g., CFL, wall shear stress) and thus did not consider CC transport. In the current work, we build off this previous work to provide new and novel insights into CC margination.

The tortuous microvessel (venule) shown in Fig. 1(b) was digitally rendered in 3D using PTC Creo,[68] and a triangular mesh was fitted to the vessel surface using Gmsh.[69] Mesh coordinates are used within the simulation approach to model the 3D complex vessel wall boundaries as previously described. The total vessel length is approximately 1 mm, and the vessel diameter is approximately 20 μm. Discussion on the reasoning behind this approach and limitations is provided later. CC transport is modeled over a range of hemodynamic conditions typical of the microcirculation, considering H_T levels of 10%, 20%, and 30%, and effective shear rates ($\dot{\gamma}_{\text{eff}} = \frac{V_{bulk}}{D}$) of 25, 50, and 100 s^{-1}. V_{bulk} is the mean velocity of the bulk blood flow and D is the vessel diameter. For each case, the volumetric flow rate is fixed at the vessel inlet to achieve the specified $\dot{\gamma}_{\text{eff}}$. The H_T level through the tortuous microvessel is initially set using an automated routine to place the desired number of RBCs, which range from 313 (10% H_T) to 942 (30% H_T). Over the course of each simulation, the overall H_T level is maintained by re-injecting RBCs at the vessel inlet when they exit the domain at the vessel outlet.

For each case, the CC is initially placed near the vessel inlet. In reality, under *in vivo* conditions, a CC could enter the vessel at any location on the cross section. From the perspective of margination, the worst-case scenario is a CC entering at the vessel centerline and we consider this position as one option for initial placement. In order to bound the CC margination analysis, we also consider the other extremum of initial position where the CC enters the vessel already in a marginated position. Prior to placing the CC, the simulation is run with RBCs for a duration corresponding to a single RBC traversing the entire length of the vessel. Furthermore, for each case considered, we also simulate five different initial RBC placements so as to ensure any conclusions on CC margination behavior are not unique to the way in which the RBCs were initially configured.

III. RESULTS AND DISCUSSION

A. Margination-like behavior occurs in the absence of RBCs due to vessel tortuosity

To establish context for CC margination behavior with RBCs, simulation data for a CC flowing without RBCs are first presented. Figure 2 provides a depiction from a representative simulation, showing how, even in the absence of RBCs, the CC will flow closer to the

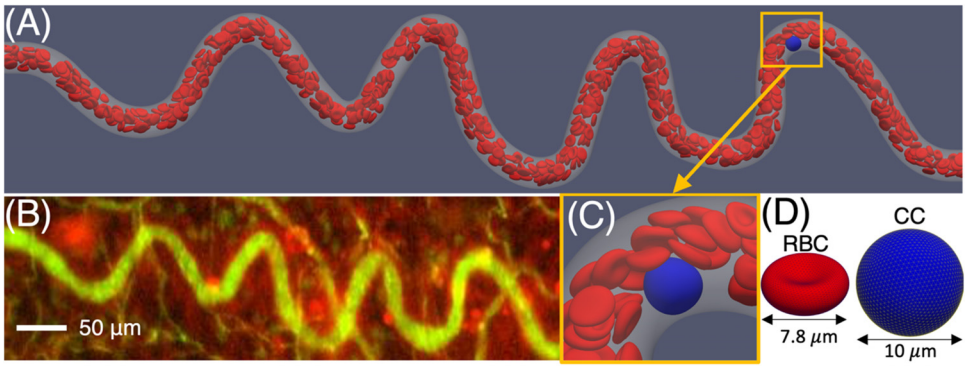

FIG. 1. Overview of CC transport simulations in a tortuous microvessel. (a) Simulation snapshot for a representative case at 20% H_T, showing the CC (blue) flowing with the RBCs (red), (b) *in vivo* image of the tortuous microvessel, (c) zoomed-in view of a marginated CC near the high curvature side of the vessel, and (d) undeformed RBC and CC shapes.

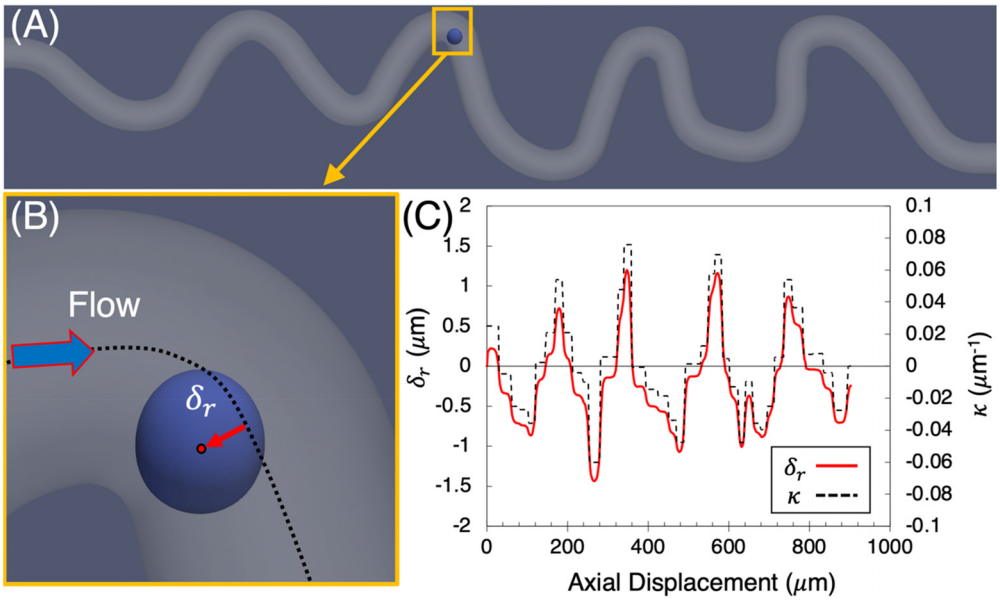

FIG. 2. Cross-stream CC migration due to vessel curvature in the absence of RBCs. (a) Overview of representative simulation of CC transport without RBCs, (b) schematic illustrating the definition of lateral displacement (δ_r) of the CC centroid from the vessel centerline, and (c) δ_r (red curve) and vessel centerline curvature (κ, black dashed curve) vs axial displacement along the vessel length, demonstrating how lateral CC migration follows the local curvature as the cell traverses the vessel.

side of the vessel with the larger local curvature. This lateral migration behavior is quantified in Fig. 2(c), where the red curve shows the CC lateral displacement (δ_r) vs vessel length, and the dashed curve is the vessel's centerline curvature (κ). It can be seen that there is transverse migration which closely follows the local curvature. The direction of this migration is purely in the plane of the curvature, or the plane of the vessel centerline.

The sign convention for κ in Fig. 2(c) is such that positive values reflect the vessel bending to the right and negative values reflect the vessel bending to the left. This designation is from the perspective of standing on the vessel centerline and looking downstream in the flow direction. Figure 2 thus demonstrates for the modeled vessel that the vessel bending to the right causes the CC to migrate laterally to the right side of the vessel and vice versa. This margination-like behavior in the absence of RBCs is expected based on recent work which demonstrated how vessel curvature causes a lateral migration of deformable cells at low Reynolds number[25,26] toward the side of the vessel with higher curvature. Under such conditions, the fluid velocity profile is skewed toward the higher curvature side of the vessel, and thus, the location of minimum shear rate over the cross section will be shifted to this same side. Deformable cells tend to migrate laterally in the direction of decreasing shear rate, which explains the behavior observed in Fig. 2(c) as the local centerline curvature oscillates along the length of the vessel.

While the data in Fig. 2 demonstrate how tortuosity can cause wall-directed CC movement in the absence of RBCs, it importantly also shows how the curvature variations inherent to a tortuous vessel cause CC movement both toward and away from a particular side of the vessel. Thus, the observation that tortuosity causes margination-like behavior is not a straightforward indicator as to whether tortuosity will enhance or diminish CC margination when flowing with RBCs in a microvessel with this morphology. Yet, isolating the impact of vessel shape alone on cross-stream CC movement is important prior to including interactions with RBCs in order to enable a more comprehensive understanding of the mechanisms underlying margination in an *in vivo* environment.

B. Establishing a margination plane for complex vessels

In the presence of RBCs, lateral CC migration can be in or out of the plane of the vessel curvature due to interactions with the RBCs. To consistently quantify and analyze margination behavior for all of the simulations given the complex geometry, we introduce a margination plane local to the instantaneous CC position. This plane is defined in such a way that it intersects both the CC centroid and the centerline of the vessel closest to the instantaneous CC centroid, and is oriented tangent to the local mean flow direction. To achieve this configuration, there are two rotations as described in Fig. 3: one to orient this plane in the flow direction while remaining in the plane of the vessel centerline [angle ϕ in Fig. 3(a)], and another to rotate out of the centerline plane [angle θ in Fig. 3(b)]. The resulting coordinate system is centered on the vessel centerline and is the plane in which the local cross-stream movement occurs. For reference, if $\theta = 0$, the lateral movement is entirely in the curvature plane, and if $\theta = \frac{\pi}{2}$, the lateral movement is normal to the curvature plane. This margination plane provides a means of comparing behavior among all cases and facilitates quantifying time-averaged behavior accounting for the CC moving past regions of varying degrees of vessel curvature.

With the margination plane defined, CC residence time at locations on the vessel cross section can be determined to elucidate margination behavior for all cases considered. Figure 4 provides a

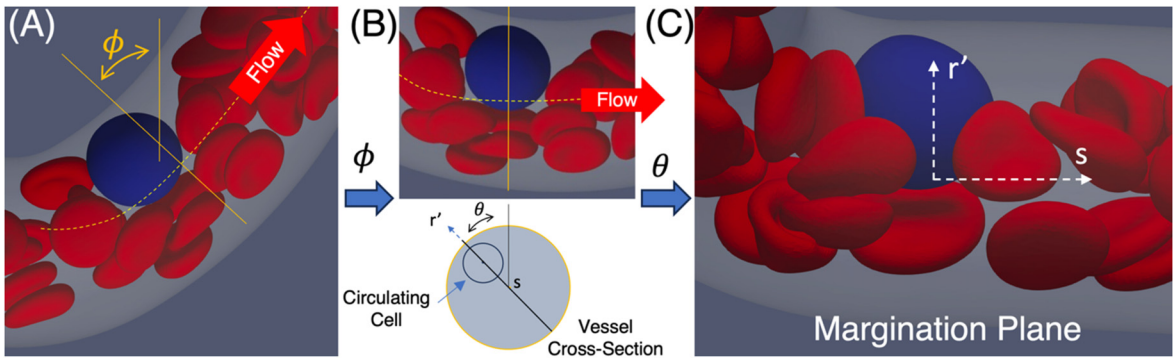

FIG. 3. Defining the margination plane for a representative CC location. (a) Region around CC at a time point in the global reference plane. ϕ is the angle between the line normal to the centerline intersecting the CC centroid and the vertical line through the CC centroid, and the red arrow gives the flow direction. (b) Rotation by ϕ in the plane of the vessel centerline (top) and depiction of the vessel cross section showing the out-of-plane location of the CC defined by angle θ (bottom), and (c) subsequent rotation by angle θ to the margination plane.

depiction of representative behavior for the case $H_T = 20\%$ and $\dot{\gamma}_{eff} = 25\,s^{-1}$. In Fig. 4(a), an overview of the simulation at an instant in time is given, showing both the RBCs (red) and the CC (blue). The red arrow gives the flow direction. In Fig. 4(b), the instantaneous CC and RBC positions are shown, rotated to the margination plane. The indicator function, which takes a value of 1.0 at Eulerian grid points inside a cell and 0.0 at Eulerian grid points outside the cell, is shown in Fig. 4(c) in the margination plane and corresponding to the cell positions in Fig. 4(b). It is noted that in Fig. 4(c), this is a 2D plane intersecting the CC centroid, and so some RBCs, which appear in Fig. 4(b) (which is a 3D perspective), may not appear in Fig. 4(c). Finally, in Fig. 4(d) contours of the indicator function time-averaged over the entire simulation are provided, which encapsulates the CC traversing the full length of the tortuous vessel. We note that for tracking and analysis, there are two different indicator functions used in the simulations, one for the RBCs and another for the CC. For ease of illustration, however no distinction is made between these separate indicator functions in Figs. 4(c) and 4(d), and the distinct shape differences between the CC and RBCs can be used to visually identify the respective regions occupied by each.

The time-averaged indicator function shown in Fig. 4(d) quantifies the fraction of time a particular location is occupied by a cell. For the CC, this shows how it tends to spend most of its time near the wall in a marginated position, while RBCs tend to occupy the center of the vessel. While the CC will move laterally in a complex trajectory as it traverses the tortuous vessel, use of the margination plane as defined here facilitates quantifying this lateral motion in a manner directly related to the margination behavior. Furthermore, this plane provides a consistent means of comparing average margination behavior between cases, and to this end, the coordinate y^* in Fig. 4(d) is used to quantify profiles across the margination plane in Sec. III C. It is also noted that viewing the CC location qualitatively in the frame of reference as shown in Fig. 4(a) can, in some cases, obscure the qualitative identification of a marginated CC for situations where this occurs more out of the plane of curvature.

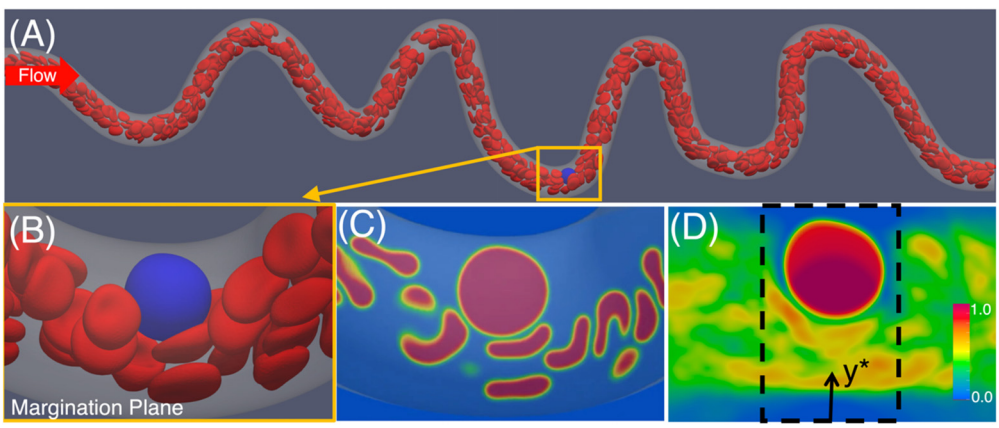

FIG. 4. Indicator function on the margination plane. (a) Snapshot of RBCs and the CC at an instant in time, for $H_T = 20\%$, $\dot{\gamma}_{eff} = 25\,s^{-1}$, (b) Local region around CC rotated to the margination plane, (c) instantaneous indicator function field on the plane through the CC centroid in (b), and (d) time-averaged indicator function in the margination plane, where coordinate y* defines the relative location across the margination plane in Fig. 5.

C. Time-averaged behavior across the margination plane

The time-averaged indicator function, as shown for the representative example in Fig. 4(d), facilitates quantifying the separate regions occupied by the RBCs and CC as the CC traverses the vessel. As mentioned, the simulations consider two different indicator functions, one for the CC and another for the RBCs. Each of these indicator functions time-averaged over each simulation is plotted in Fig. 5, and the profiles are provided as a function of distance across the margination plane. Here, the indicator function values that comprise the trends are each taken as the average at the y* location across the boxed region [see Fig. 4(d)]. To distinguish between the CC and the RBCs in Fig. 5, the indicator function for the CC is denoted with blue curves, while that for the RBCs is denoted with red curves. The plots shown in Fig. 5(a) are for simulations in which the CC is initially placed at the center of the vessel, while those in Fig. 5(b) are for the CC starting near the wall (i.e., already marginated). The sub-figures across Figs. 5(a) and 5(b) correspond to $H_T = 10\%$, 20%, and 30%, respectively, as noted in the figure. Additionally, the different line types (i.e., solid, dashed, dotted) correspond to $\dot{\gamma}_{eff} = 25$, 50, and $100\,s^{-1}$, respectively. The vertical dashed lines in the figures denote the location at which a "near-wall" region begins. As mentioned, works have reported that microvilli lengths, which facilitate cell adhesion to the vessel walls can range from 0.2 to 2 μm with a mean value of approximately 0.5 μm.[48,49] While the current work focuses on the fluid dynamics leading to and causing margination and thus does not consider cell adhesion, the physiological relevance of studying margination and the degree to which it occurs is rooted in its potential to provide an adhesion pathway. Thus, for the current work, we consider a near-wall region that is 0.5 μm from the wall.

The data in Fig. 5 provide the fraction of time a CC or the RBCs occupy a particular location across the margination plane. As evident, the CC profiles are generally shifted to the right side of each plot (i.e., closer to the wall), while the RBC profiles occupy the inverse spatial region. The CC curves tend to reach their peak at y^* locations ranging from approximately 0.7 to 0.75, with peak values slightly less than 1.0. The RBC curves reach their peak values at y^* locations of approximately 0.25 with peak magnitudes generally increasing in direct proportion to the H_T level. It is noted that the CC diameter is half of the vessel diameter, which leads to these y* locations on which each set of curves is approximately centered. The information provided by these data depicts a comprehensive residence time history over the vessel cross section associated with the respective margination behavior for each case.

A quantity of interest which emerges from Fig. 5 is the value of the time-averaged indicator function at the intersection of the vertical dashed line and the curve for each CC profile. This value is denoted here as I_{int} and quantifies the fractional near-wall residence time. First, considering cases where the CC is initially placed on the centerline of the vessel [Fig. 5(a)], I_{int} is generally observed to increase with H_T and decrease with $\dot{\gamma}_{eff}$. At 10% H_T, the smallest range of I_{int} is observed, where the values are approximately 0.17, 0.12, and 0.11 for $\dot{\gamma}_{eff} = 25$, 50, and $100\,s^{-1}$, respectively. Increasing to 20% H_T enhances both the magnitude of I_{int} and the variation across $\dot{\gamma}_{eff}$, where values of 0.35, 0.24, and 0.17 are observed for $\dot{\gamma}_{eff} = 25$, 50, and $100\,s^{-1}$, respectively.

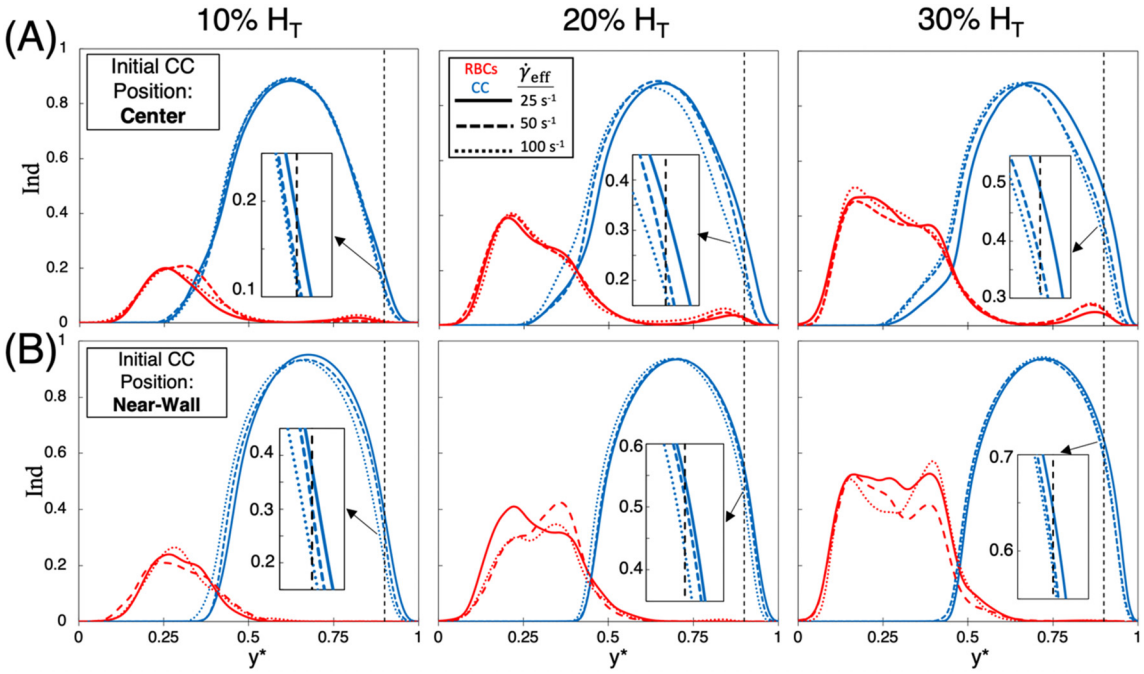

FIG. 5. Indicator function profiles across the margination plane for RBCs and the CC. (a) Cases where the CC is initially placed on the centerline of the vessel and (b) cases where the CC is initially placed near the wall. The red and blue curves provide the time-averaged indicator function for the RBCs and the CC, respectively. Profiles are plotted as a function of relative distance across the margination plane (y*) as defined in Fig. 4(d), and the different line types (solid, dashed, dotted) correspond to the noted $\dot{\gamma}_{eff}$ cases. The separate figures within (a) and (b) correspond to 10%, 20%, and 30% H_T cases, and the vertical black dashed line denotes the near-wall location.

Furthermore, I_{int} values at 30% HT are 0.52, 0.36, and 0.32 for the same respective $\dot{\gamma}_{\text{eff}}$ values.

The data in Fig. 5(a) show how the CC tends to spend more time near the wall with increasing H_T and decreasing $\dot{\gamma}_{\text{eff}}$. Increasing I_{int} with H_T can be partially attributed to the increased occupation by RBCs in the more central vessel region, as evident from the RBC indicator function trends in Fig. 5(a) and described above. This behavior is expected because it occurs in a straight tube as well. Mechanisms deriving from the vessel tortuosity, however, also contribute to the behavior. First, the increased presence of RBCs inherent to increasing H_T dampens the lateral CC movement in response to tortuosity. Namely, once the CC reaches the wall, it stays there with increasing tendency in direct proportion to H_T. Second, increasing $\dot{\gamma}_{\text{eff}}$ increases the slope of the cross-sectional velocity profile resulting in sharper changes to the local shear rate profile over the vessel cross section. As mentioned, deformable cells laterally migrate in the direction of decreasing local shear rate, and with increasing flow strength (i.e., increasing $\dot{\gamma}_{\text{eff}}$), there will be increased rate of lateral movement of the CC. For the tortuous microvessel, this behavior with increasing $\dot{\gamma}_{\text{eff}}$ manifests as enhanced movement following the local vessel curvature, which causes the CC to increasingly move in and out of the near-wall region. Considering these tortuosity-derived mechanisms together results in the observed behavior. That is, at 10% H_T the RBC dampening effect is lowest permitting more lateral CC movement out of the near-wall region following the local curvature. This behavior results in comparatively lower I_{int} magnitudes overall for the 10% H_T cases, while within this H_T level I_{int} increases as $\dot{\gamma}_{\text{eff}}$ drops due to less motion out of the near-wall region. For 20% and 30% H_T, the RBC dampening effect progressively increases resulting in greater I_{int} magnitudes, and within each H_T level, the tortuosity-driven CC movement out of the near-wall region increases with $\dot{\gamma}_{\text{eff}}$. Furthermore, evidence and quantification of tortuosity-derived mechanisms are provided in Sec. III D. Altogether, the behavior observed in Fig. 5(a) where the CC starts on the centerline of the vessel shows how once the CC is able to move into a near-wall region, it has an increasing tendency to stay there with increasing RBC volume fraction. For each H_T level, increasing $\dot{\gamma}_{\text{eff}}$ tends to pull the CC out of the near-wall region more easily in response to tortuosity.

When considering actual *in vivo* behavior, a CC can enter a vessel at any location on the vessel cross section. From the perspective of margination, the worst-case scenario is then a CC entering at the vessel centerline and hence the simulations represented by the data in Fig. 5(a). These data include behavior both prior to and after the CC first reaches the near-wall location, and importantly shows how, at a bare minimum, the CC will reach the wall during transport. Yet, once a CC reaches the wall of a tortuous microvessel to what degree will it remain marginated? In order to answer this question and bound the CC margination analysis, we also consider the other extremum of initial position where the CC enters the vessel at a near-wall location. The time-averaged indicator function for these cases is presented in Fig. 5(b). In general, the behavior is qualitatively similar to that of Fig. 5(a), with the major differences being the I_{int} magnitudes are higher between equivalent cases in 5B vs 5A, and the I_{int} variation across $\dot{\gamma}_{\text{eff}}$ for a particular H_T level is reduced. The minor differences in the blue curves for each sub-figure indicates that $\dot{\gamma}_{\text{eff}}$ has a small influence on sustained margination. Overall, as H_T increases from 10% to 30%, the fraction of time spent in the near-wall region increases from 0.3 to 0.7. These data support our observation above for the cases involving the CC initially placed at the centerline, where once a CC enters the near-wall region its tendency to remain there generally increases with increasing H_T.

D. CC margination to the cell-free layer vs near-wall and connection to tortuosity

As a CC migrates laterally toward the vessel walls, the cell surface first enters the CFL and subsequently moves closer to the wall. While the CFL is inherently a near-wall region, its thickness in the microcirculation typically can range from approximately 0.5 to 5 μm as has been observed *in vivo*[40–44] as well as in high-fidelity 3D simulations.[25,46] Considering the range of microvilli lengths previously mentioned and the overlap with this range of CFL thickness values, we quantify CC margination behavior in terms of both margination to the CFL as well as the near-wall region previously defined in order to provide a more comprehensive analysis.

Figure 6 provides a representative CC trajectory for $H_T = 20\%$ and $\dot{\gamma}_{\text{eff}} = 50\,\text{s}^{-1}$ to illustrate observed margination behavior unique to the tortuous microvessel, considering both the CFL and the near-wall region. The solid black line gives the radial displacement of the CC centroid vs axial displacement, and the orange shading represents the trajectory differences among the different initial RBCs configurations. As shown, we generally observe negligible differences in lateral migration behavior based on the initial configuration of RBCs placed throughout the vessel. The shape of the CFL is complex, asymmetric, and 3D, and the high-fidelity simulations enable calculation of the detailed geometrical characteristics for each H_T and $\dot{\gamma}_{\text{eff}}$ case. These data were reported in a recent work focused on studying the hemodynamic characteristics unique to a tortuous microvessel[46] and are utilized here to aid in the CC margination analysis. In Fig. 6, the time-averaged RBC core boundary is provided which marks the beginning of the CFL and provides a means of visually depicting the boundary relative to the local CC lateral position. Also shown in the figure are the near-wall region 0.5 μm from the wall and the local vessel curvature κ. Since CC lateral movement from the vessel centerline into the near-wall region was observed across all cases [Fig. 5(a) and associated discussion], Fig. 6 considers a CC initially placed near the vessel wall in order to focus on lateral movement behavior once the CC reaches the CFL.

The data in Fig. 6 depict behavior we generally observe for all cases, albeit to varying degrees. Namely, once the cell surface enters the near-wall region, the cell will tend to move in and out of this region following the local vessel curvature. This tendency is evident by qualitatively comparing the CC radial displacement (black curve) with the vessel curvature (dashed black curve); local increases in trajectory (i.e., motion toward the wall) correspond to local increases in curvature (i.e., high curvature on the vessel side nearest the local cell location) and vice versa. This behavior is quantified by computing the correlation coefficient between the radial displacement during transport (r') and the corresponding local curvature value (κ):

$$C_{r'-\kappa} = \frac{\sum_{i=1}^{n}\left(r'_i - \bar{r}'\right)\left(\kappa_i - \bar{\kappa}\right)}{\sqrt{\sum_{i=1}^{n}\left(r'_i - \bar{r}'\right)^2}\sqrt{\sum_{i=1}^{n}\left(\kappa_i - \bar{\kappa}\right)^2}}, \tag{12}$$

where the subscript i denotes the quantity corresponding to an individual CC location along the length, n gives the total number of points

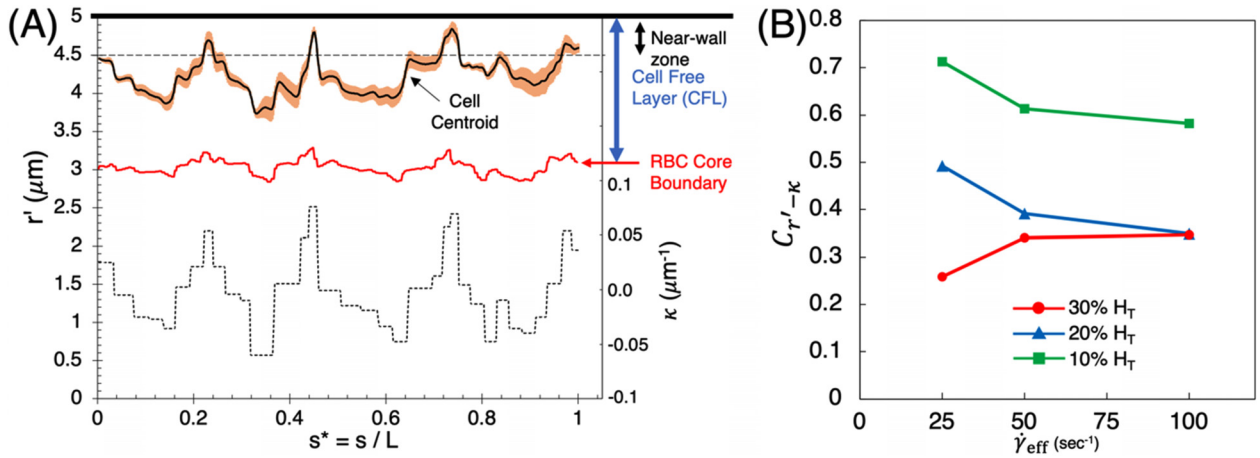

FIG. 6. Margination behavior and influence of tortuosity. (a) CC margination to the CFL and near-wall zone vs axial displacement along the vessel, for $H_T = 20\%$ and $\dot{\gamma}_{eff} = 50\,s^{-1}$. s is the axial displacement along the vessel of length L and r' is the lateral displacement from the centerline. The black curve gives the lateral displacement of the CC centroid, and the orange shading represents trajectory differences for different initial RBC configurations around the CC. Furthermore, the red line provides the RBC core boundary, and the black dotted line gives the local vessel curvature (κ). (b) Correlation coefficient between r' and κ, for all cases as a function of $\dot{\gamma}_{eff}$.

along the length at which local data were measured (on the order of 1000), and the overbar denotes the average among all measurements over the length. As a point of reference, $C_{r'-\kappa}$ is approximately 0.35 for the r' and κ curves in Fig. 6(a).

$C_{r'-\kappa}$ values for all cases are presented in Fig. 6(b), which elucidates the connection between marginated CC lateral migration behavior and tortuosity across varying hemodynamics conditions typical of the microcirculation. Recent work showed how, in the absence of RBCs, increasing $\dot{\gamma}_{eff}$ will effectively increase the rate of lateral migration due to vessel curvature.[26] In the presence of RBCs, the connection between lateral migration in response to κ becomes more complex. The data in Fig. 6(b) reflect an observed interplay between $\dot{\gamma}_{eff}$ (and resulting shear rate profile over the cross section), axial distance between regions in which the curvature changes, and RBC volume fraction. At 10% H_T, the CC is able to laterally move most freely, and thus, the largest $C_{r'-\kappa}$ values are observed. $C_{r'-\kappa}$ is largest (0.71) at $25\,s^{-1}$ and decreases to 0.6 at $100\,s^{-1}$. At the lower $\dot{\gamma}_{eff}$, the axial velocity is also smallest, and thus, the CC transit time from one bend to the next enables the CC to more closely follow the curvature before it changes again at the next bend. With increasing $\dot{\gamma}_{eff}$ and increasing axial velocity, the CC transport time between bends increases resulting in the slightly diminished $C_{r'-\kappa}$. With H_T increasing to 20%, the RBC dampening becomes more pronounced, thus reducing $C_{r'-\kappa}$ compared to 10% H_T. $C_{r'-\kappa}$ values similarly decrease with $\dot{\gamma}_{eff}$, from 0.5 at $25\,s^{-1}$ to 0.35 at $100\,s^{-1}$. At 30% H_T, $C_{r'-\kappa}$ is further reduced, except now $C_{r'-\kappa}$ interestingly increases with $\dot{\gamma}_{eff}$. These data indicate an H_T threshold exists, whereby once the RBC volume fraction becomes sufficiently high the RBCs tightly lock the CC near the wall. Lateral movement under such conditions then increases in response to the near-wall RBC presence, which is directly related to the CFL thickness. The CFL thickness increases with $\dot{\gamma}_{eff}$,[46] which results in the observed CC lateral migration behavior reflected in Fig. 6(b) for 30% H_T.

In terms of CC residence in the CFL, the trajectory in Fig. 6(a) reveals how the CC surface remains in the CFL for the entirety of its transport through the vessel. This behavior is important to note because it indicates that the CC surface remains exposed to the endothelium over the entire length of the vessel. Given the heterogeneity of possible receptor lengths noted above, this finding has important implications for understanding why CCs may adhere and extravasate in microvascular regions with tortuous morphologies. Furthermore, the boundary of the RBC core in Fig. 6(a) can be seen to qualitatively follow the local vessel curvature. Compared to the CC lateral migration behavior without RBCs shown in Fig. 3 where the CC moves back and forth between sides of the vessel, Fig. 6(a) demonstrates how (i) the RBCs also shift laterally due to the tortuosity and (ii) the collective movement with the CC creates the above-noted mechanism to effectively lock the CC in the CFL.

To quantify and compare CFL vs near-wall residence time among all cases, we define the parameter α, which gives the fraction of time spent in the CFL (α_{CFL}) or near-wall region (α_{NW}) as the CC traverses the vessel. It is noted that α_{NW} is identical to the near-wall time fraction (I_{int}) discussed in Sec. III C and is provided here for context when considering CFL residence. Figure 7(a) provides α values for cases where the CC is initially placed on the vessel centerline, and Fig. 7(b) provides values for cases where the CC is initially placed near the wall. The data point for each case represents the average of 5 separate simulations with identical hemodynamic conditions (H_T and $\dot{\gamma}_{eff}$) but different initial RBC configurations.

For a CC initially placed on the vessel centerline, Fig. 7(a) shows how α_{CFL} is greater than α_{NW} for all cases. This behavior is expected because the CC must laterally migrate through the CFL to reach the near-wall region. The data for α_{NW} reiterates the quantifications and discussion in Sec. III C, where α_{NW} generally increases with increasing H_T and decreasing $\dot{\gamma}_{eff}$. In contrast, α_{CFL} generally falls within the range of 0.6–0.7 without any clear dependence on H_T and $\dot{\gamma}_{eff}$. This is likely caused by the fact that the CFL thickness varies with H_T and $\dot{\gamma}_{eff}$, whereas the demarcation of the near-wall region is constant. Additionally, within each individual H_T-$\dot{\gamma}_{eff}$ case, the CFL is highly heterogenous and asymmetric along the vessel. Taking these considerations together, the computation of CC time fraction within a region

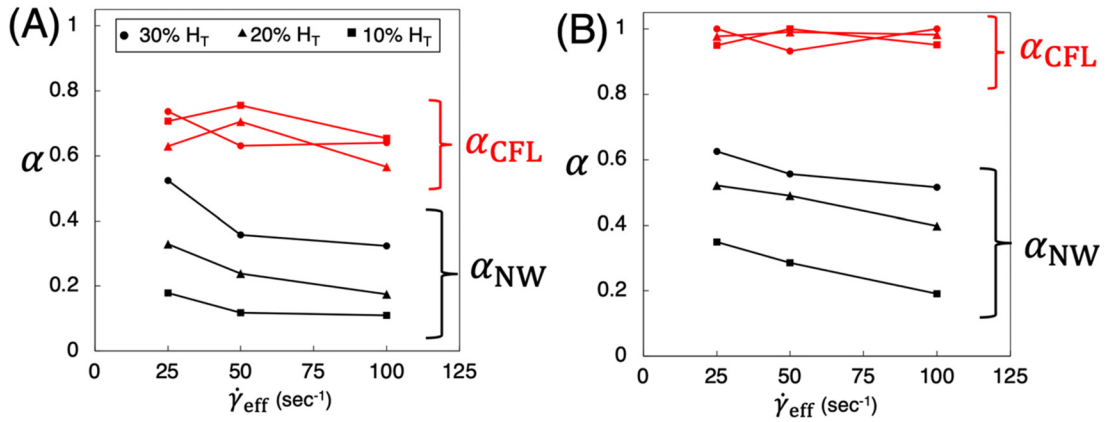

FIG. 7. CC time fractions (alpha) in the CFL vs near-wall regions during CC traversal of the tortuous microvessel. (a) CC is initially placed on the vessel centerline, and (b) CC is initially placed near the wall. For (a) and (b), α_{NW} gives the fraction of time spent in the near-wall region and α_{CFL} gives the fraction of time spent in the CFL. The x-axis is the effective shear rate ($\dot{\gamma}_{eff}$) for the case, and the individual curves represent the noted H_T value.

whose boundary is also influenced by hemodynamic conditions likely mitigates dependence on those hemodynamic conditions and leads to the observed behavior for α_{CFL}.

The data in Fig. 7(b) for a CC initially placed near the wall show a similar relationship between α_{CFL} and α_{NW} as that of Fig. 7(a), whereby α_{CFL} is greater than α_{NW} for all cases as expected. The data, however, also importantly provide quantitative evidence that once the CC reaches the wall, the RBCs effectively lock the CC in the CFL as previously noted. This behavior is as evident from the red data points in Fig. 7(b), which are all very close to 1.0. Thus, the representative behavior depicted in Fig. 6(a) for CFL residence holds across the range of hemodynamic conditions considered.

E. Differences in margination behavior between a tortuous microvessel and straight tube

The findings presented in previous sections, which quantify how margination is observed in the tortuous microvessel for all H_T and $\dot{\gamma}_{eff}$ values considered, are different from what occurs in a straight tube. Notably, simulations we have performed for CC margination in a straight tube (see supplementary material), which agree with those reported elsewhere,[15] do not predict CC margination for regions of the parameter space we have explored, particularly at the 10% H_T level. To directly quantify differences in margination behavior between the tortuous in microvessel and an idealized straight tube, we define the parameter β as

$$\beta = \frac{\alpha^{\text{tortuous}}}{\alpha^{\text{straight}}}, \tag{13}$$

where the superscript for each α value denotes the vessel type associated with the respective time fraction. Following the analysis in Sec. III D, we consider both β_{NW} and β_{CFL} in order to best elucidate differences in margination behavior to the near-wall vs CFL.

In Fig. 8, β values for all cases are provided, where β_{NW} [Fig. 8(a)] and β_{CFL} [Fig. 8(b)] are plotted vs $\dot{\gamma}_{eff}$ and each curve corresponds to the noted H_T value. In each figure, the yellow highlighted region represents β values greater than 1.0, which indicates margination is enhanced relative to the equivalent straight tube case. For the

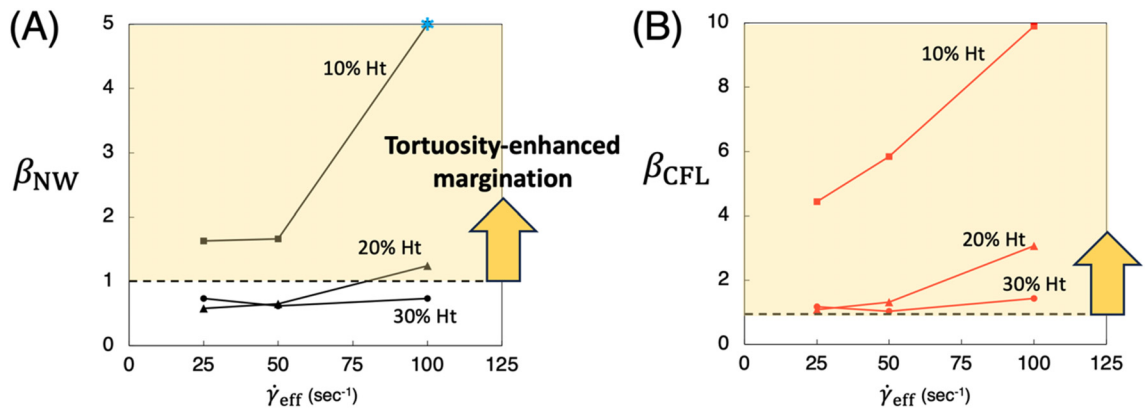

FIG. 8. Comparing CC residence time between the tortuous microvessel and that observed in a straight tube. Here, $\beta = \frac{\alpha^{\text{tortuous}}}{\alpha^{\text{straight}}}$, where (a) is for the near-wall region (β_{NW}) and (b) is for the CFL (β_{CFL}). The yellow shaded areas represent parameter combinations where residence time is enhanced by tortuosity.

near-wall behavior shown in Fig. 8(a), the near-wall CC residence time is greater for all 10% H_T cases, as well as for 20% H_T, $\dot{\gamma}_{eff} = 100\,s^{-1}$. It is noted that the 10% H_T, $\dot{\gamma}_{eff} = 100\,s^{-1}$ case is marked with an asterisk because this parameter combination resulted in near-zero margination for the straight tube, and a $\beta = 5$ value was used for visualization purposes in the figure. For the other cases at 20% H_T and all 30% H_T cases, the near-wall residence time was reduced compared to the straight tube. In contrast, when considering CC residence time in the CFL Fig. 8(b) indicates that for all H_T and $\dot{\gamma}_{eff}$ values, the CC residence time is increased compared to behavior in a straight tube.

In terms of near-wall CC residence time and behavior, the data in Fig. 8(a) show how tortuosity can have a mixed impact in terms of either enhancing or diminishing margination relative to a straight tube. On the one hand, we observe that tortuosity provides a mechanism that can enable cells to marginate for cases in which they would not marginate in a straight vessel. On the other hand, for cases in which a cell can already easily marginate in a straight tube, as the CC traverses a tortuous vessel and enters and exits regions of high curvature, the changing local geometry can temporarily pull the CC away from the wall which would not happen in a straight tube. In terms of CC residence time in the CFL, the data in Fig. 8(b) show how for all cases the residence time is enhanced by tortuosity. This is most notable at 10% H_T, and to a lesser degree at 20% and 30% H_T. So, while the local vessel curvature can pull the CC in and out of the near-wall region, these data on CFL residence time compared to a straight tube provide an additional perspective extending the observations accompanying Fig. 7(b). Namely, not only does a CC tend to stay in the CFL once it gets there, but importantly this is fundamentally different from what occurs in a straight tube.

To date, simulations in idealized straight tubes have provided important mechanistic insight into the margination phenomena. Yet, the straight tube geometry is significantly different than commonly observed *in vivo* vessel morphologies such as the tortuous microvessel that has been studied here. Elucidating differences between the current findings and that predicted for straight tubes helps to build a more complete understanding of the phenomena as it likely occurs *in vivo*.

IV. ADDITIONAL DISCUSSION AND LIMITATIONS

The underlying goal of the current work is to provide new mechanistic insights into the role played by tortuosity in influencing CC margination behavior. While different approaches could be taken toward addressing this goal such as considering an idealized geometry with a single bend and periodic boundary conditions, here we opted to model a tortuous microvessel based on *in vivo* images over a relatively long length. In this context, thus the question was posed: if a CC was in this actual vessel, what would happen with regard to margination behavior? To aid in answering this question and account for heterogeneity of hemodynamic conditions typical of the microcirculation, initial CC positions both on the vessel centerline and near the vessel wall were considered in order to bound the analysis, along with different physiological $\dot{\gamma}_{eff}$ and H_T levels. The current work thus represents a combination of parametric analysis sweeping a range of influencing parameters and a fixed vessel geometry. Effects of vessel diameter or specific vessel curvature values are not considered. Interestingly, the results in Sec. III A suggest that in vessels with smaller diameters than that considered here, the curvature alone may be sufficient to cause pronounced near-wall behavior leading to adhesion even without RBCs. Additional studies are needed however to address such possibilities.

While a tortuous vessel based on *in vivo* images was the basis for the presented analysis, simplifications and assumptions were made in order to aid in identifying the specific role of tortuosity. For example, close inspection of the *in vivo* image in Fig. 1(b) shows that the vessel diameter is not perfectly constant along the length. Similarly, while not evident from the 2D image, the cross-sectional shape may not be perfectly circular. Furthermore, local endothelial cell shapes forming the interior surface of the vessel are not accounted for. Inclusion of such geometrical features may slightly alter local CC behavior and affect the specific near-wall CC distances observed. Yet, the main conclusions of this work on the role of tortuosity itself would not change.

The physical mechanisms which drive differences between the tortuous microvessel and straight tube in large part derive from the difference between the undisturbed velocity profile in a curved tube vs a straight tube. In a straight tube, the velocity profile over the cross section follows that for Poiseuille flow; the profile is symmetric about the centerline where both the maximum velocity and location of minimum local shear rate occur at the vessel center. In a curved tube, the velocity profile is not symmetric about the centerline but rather at low Re is shifted toward the side of the vessel with the higher curvature, meaning the location of minimum local shear rate is closer to the side of the vessel with the higher curvature.[20–23,25] This location of minimum shear is important because a deformable cell will tend to laterally migrate toward this location.[24] In the context of CC margination considered here, the curvature-based mechanism will affect both the RBCs and the CC.

In a tortuous microvessel which bends back and forth, the local curvature oscillates along the length of the vessel. For a single CC without RBCs, the corresponding shift of the location of minimum shear on the cross section will cause the CC to laterally migrate back and forth to the vessel side with higher local curvature [Fig. 2(c)]. A suspension of highly deformable RBCs will also laterally migrate following the local curvature, and the cumulative effects of this behavior and the cell–cell interactions result in locally varying and asymmetric CFL shapes with CFL thickness being smaller on the side of the vessel with higher curvature.[46] The CC margination observed for the tortuous microvessel essentially results from a superposition of these two scenarios. Isolating behavioral differences compared to a straight tube can be conceptualized by first considering an underlying mechanism present in both morphologies. Namely, for CC flowing with a suspension of highly deformable RBCs, regardless of the vessel shape the RBCs will tend to displace the CC toward the margins of the vessel. If vessel curvature is subsequently considered, the additional curvature-derived mechanism driving lateral migration will be present. The observations in the current work elucidate a complex integration of these contributors and over a range of conditions.

RBC aggregation is not considered in the current work. While this phenomenon has been shown to enhance CC margination,[2,9,15,17,50,51] as mentioned works have shown this phenomenon is not necessary for a CC to marginate and the current findings confirm this observation for the tortuous microvessel considered. The means by which RBC aggregation affects margination in a tortuous microvessel, however, represents an important physiological question. Owing to the computational cost of the 3D cell-resolved simulations and the parameter space increase needed to include aggregation, here we have

focused purely on the hydrodynamic mechanisms. Future work is warranted to quantify the role played by aggregation. In a similar spirit, we also do not consider CC adhesion. Such omission is in part due to computational cost, but also importantly in order to elucidate margination behavior solely due to fluid mechanics-derived cell-scale behavior and interactions. Such findings provoke future studies modeling CC adhesion in RBC-resolved tortuous *in vivo* microvessels to address important physiological questions related to probable CC attachment sites, associated cell-scale dynamics, and connections to specific microvessel morphologies.

The model employed for the CC neglects viscoelasticity. While incorporating viscoelasticity could improve the fidelity of the model, we do not feel the scale of this improvement would change any of the main conclusions of this work. Recent works that have demonstrated viscoelastic behavior have considered, for example, squeezing through microfluidic devices,[70,71] atomic force microscopy (AFM) probing *in vitro*,[72] or cell motility in tissue,[73,74] which are more related to the relatively slow migration of cells through highly confined environments. Under these circumstances, the CC undergoes relatively large deformations and over different timescales compared to the current work where our focus is on CC transport behavior with a suspension of RBCs flowing through a microvessel. Under the conditions that we consider in the current work, our CC model is sufficient to predict the margination phenomena and our straight tube results agree with that of others.[15] We also note that, when considering CC transport behavior, recent work[31] has shown how this type of CC model can recreate transport behavior of specific cancer cell lines without requiring viscoelasticity, further justifying the reasonable use of this model in the current work.

V. SUMMARY AND CONCLUSIONS

This work has presented quantification and analysis of CC margination in a tortuous microvessel digitally reconstructed based on *in vivo* images. To our knowledge, this is the first study to elucidate margination behavior under such conditions based on 3D RBC- and CC-resolved simulations. First, in the absence of RBCs, we show how a CC laterally migrates in response to local vessel curvature. While such behavior is expected based on recent work,[26,55] the degree to which it occurs for the tortuous microvessel studied here importantly suggests that in smaller diameter microvessels, tortuosity can provide a means for a CC surface to reach the endothelium even without RBCs. Next, considering a range of physiological conditions typical of the microcirculation, detailed analysis shows how the CC is able to marginate for all H_T and $\dot{\gamma}_{eff}$ cases considered. Through defining a local margination plane unique to the complex vessel shape, we have quantified where on the vessel cross section the CC tends to reside with respect to margination. Such data are used to elucidate how the hemodynamic conditions coupled with the tortuosity cause the degree of CC margination to generally increase with H_T (10%–30%) and decrease with $\dot{\gamma}_{eff}$ (25–100 s^{-1}). Moreover, detailed calculation of the 3D CFL shape enabled characterizing CC margination in terms of both entering the CFL vs flowing immediately adjacent to the wall. Importantly, we observe that once the CC surface reaches the CFL it will tend to remain there across all conditions tested. Such characterization is physiologically important with respect to elucidating potential for CC adhesion. Finally, the data notably show how compared to margination behavior in a straight tube, the presence of vessel tortuosity can have something of a balancing effect. On the one hand, at low H_T (10%), vessel tortuosity provides a mechanism enabling CCs to reach the wall. This extra wall-directed movement either enhances the degree of CC margination compared to a straight tube or, under some conditions, enables margination to occur where it would not occur in a straight tube. On the other hand, at higher H_T levels (20–30%) where margination can already easily occur in a straight tube, tortuosity can slightly reduce the degree of margination by temporarily pulling the CC away from the wall in regions of high local curvature. Altogether, this work provides a new characterization of the margination phenomenon by considering microvessel tortuosity. The findings importantly establish a foundation for future work investigating the causal roles played by microvascular geometry, and further toward enabling prediction of CC transport and attachment in the vascular tree.

SUPPLEMENTARY MATERIALS

See the supplementary material for provided which includes simulations of CC margination in a straight tube and validation.

ACKNOWLEDGMENTS

This work is supported by a grant (No. CBET 2309559) from the National Science Foundation.

This work used Expanse at the San Diego Supercomputer Center through Allocation No. MCH220044 from the Advanced Cyberinfrastructure Coordination Ecosystem: Services & Support (ACCESS) program,[75] which is supported by National Science Foundation Grant Nos. 2138259, 2138286, 2138307, 2137603, and 2138296. Additional computational resources on Wulver at the New Jersey Institute of Technology are acknowledged.

AUTHOR DECLARATIONS

Conflict of Interest

The authors have no conflicts to disclose.

Author Contributions

Ali Kazempour: Data curation (equal); Formal analysis (equal); Investigation (equal); Visualization (equal); Writing – original draft (equal). **Peter Balogh:** Conceptualization (equal); Investigation (equal); Methodology (equal); Supervision (equal); Writing – original draft (equal).

DATA AVAILABILITY

The data that support the findings of this study are available from the corresponding author upon reasonable request.

REFERENCES

[1]R. F. Tuma, W. N. Durán, and K. Ley, *Microcirculation* (Academic Press, 2011), Vol. 4.

[2]J. C. Firrell and H. H. Lipowsky, "Leukocyte margination and deformation in mesenteric venules of rat," Am. J. Physiol.: Heart Circ. Physiol. **256**, H1667–H1674 (1989).

[3]M. R. King *et al.*, "A physical sciences network characterization of circulating tumor cell aggregate transport," Am. J. Physiol.: Cell Physiol. **308**, C792–C802 (2015).

[4]U. Bagge, P. Brånemark, R. Karlsson, and R. Skalak, "Three-dimensional observations of red blood cell deformation in capillaries," Blood Cells **6**, 231–239 (1980).

[5]H. L. Goldsmith and S. Spain, "Margination of leukocytes in blood flow through small tubes," Microvasc. Res. **27**, 204–222 (1984).
[6]I. Cantat and C. Misbah, "Lift force and dynamical unbinding of adhering vesicles under shear flow," Phys. Rev. Lett. **83**, 880 (1999).
[7]M. Abkarian, C. Lartigue, and A. Viallat, "Tank treading and unbinding of deformable vesicles in shear flow: Determination of the lift force," Phys. Rev. Lett. **88**, 068103 (2002).
[8]S. Meßlinger, B. Schmidt, H. Noguchi, and G. Gompper, "Dynamical regimes and hydrodynamic lift of viscous vesicles under shear," Phys. Rev. E **80**, 011901 (2009).
[9]M. J. Pearson and H. H. Lipowsky, "Influence of erythrocyte aggregation on leukocyte margination in postcapillary venules of rat mesentery," Am. J. Physiol.: Heart Circ. Physiol. **279**, H1460–H1471 (2000).
[10]G. W. Schmid-Schönbein, S. Usami, R. Skalak, and S. Chien, "The interaction of leukocytes and erythrocytes in capillary and postcapillary vessels," Microvasc. Res. **19**, 45–70 (1980).
[11]E. Bullitt, K. E. Muller, I. Jung, W. Lin, and S. Aylward, "Analyzing attributes of vessel populations," Med. Image Anal. **9**, 39–49 (2005).
[12]D. C. Chong, Z. Yu, H. E. Brighton, J. E. Bear, and V. L. Bautch, "Tortuous microvessels contribute to wound healing via sprouting angiogenesis," Arterioscler., Thromb., Vasc. Biol. **37**, 1903–1912 (2017).
[13]F. Gekeler, K. Shinoda, M. Jünger, K. U. Bartz-Schmidt, and F. Gelisken, "Familial retinal arterial tortuosity associated with tortuosity in nail bed capillaries," Arch. Ophthalmol. **124**, 1492–1494 (2006).
[14]R. J. Tapp *et al.*, "Retinal vascular tortuosity and diameter associations with adiposity and components of body composition," Obesity **28**, 1750–1760 (2020).
[15]D. A. Fedosov and G. Gompper, "White blood cell margination in microcirculation," Soft Matter **10**, 2961–2970 (2014).
[16]J. B. Freund, "Leukocyte margination in a model microvessel," Phys. Fluids **19**, 023301 (2007).
[17]A. Jain and L. L. Munn, "Determinants of leukocyte margination in rectangular microchannels," PLoS One **4**, e7104 (2009).
[18]C. Sun, C. Migliorini, and L. L. Munn, "Red blood cells initiate leukocyte rolling in postcapillary expansions: A lattice Boltzmann analysis," Biophys. J. **85**, 208–222 (2003).
[19]T. W. Secomb, "Blood flow in the microcirculation," Annu. Rev. Fluid Mech. **49**, 443–461 (2017).
[20]S. Murata, Y. Miyake, and T. Inaba, "Laminar flow in a curved pipe with varying curvature," J. Fluid Mech. **73**, 735–752 (1976).
[21]R. Chadwick, "Slow viscous flow inside a torus—The resistance of small tortuous blood vessels," Q. Appl. Math. **43**, 317–323 (1985).
[22]C. Wang and J. Bassingthwaighte, "Blood flow in small curved tubes," J. Biomech. Eng. **125**, 910–913 (2003).
[23]A. Verkaik, B. Beulen, A. Bogaerds, M. Rutten, and F. Van De Vosse, "Estimation of volume flow in curved tubes based on analytical and computational analysis of axial velocity profiles," Phys. Fluids **21**, 023602 (2009).
[24]G. Coupier, B. Kaoui, T. Podgorski, and C. Misbah, "Noninertial lateral migration of vesicles in bounded Poiseuille flow," Phys. Fluids **20**, 111702 (2008).
[25]P. Balogh and P. Bagchi, "The cell-free layer in simulated microvascular networks," J. Fluid Mech. **864**, 768–806 (2019).
[26]S. Ebrahimi, P. Balogh, and P. Bagchi, "Motion of a capsule in a curved tube," J. Fluid Mech. **907**, A28 (2021).
[27]N. Takeishi, Y. Imai, K. Nakaaki, T. Yamaguchi, and T. Ishikawa, "Leukocyte margination at arteriole shear rate," Physiol. Rep. **2**, e12037 (2014).
[28]A. H. Isfahani and J. B. Freund, "Forces on a wall-bound leukocyte in a small vessel due to red cells in the blood stream," Biophys. J. **103**, 1604–1615 (2012).
[29]W. Yan, Y. Liu, and B. Fu, "Effects of curvature and cell–cell interaction on cell adhesion in microvessels," Biomech. Model. Mechanobiol. **9**, 629–640 (2010).
[30]S. Wang, T. Ye, G. Li, X. Zhang, and H. Shi, "Margination and adhesion dynamics of tumor cells in a real microvascular network," PLoS Comput. Biol. **17**, e1008746 (2021).
[31]P. Balogh, J. Gounley, S. Roychowdhury, and A. Randles, "A data-driven approach to modeling cancer cell mechanics during microcirculatory transport," Sci. Rep. **11**, 15232 (2021).
[32]A. Glenn and C. E. Armstrong, "Physiology of red and white blood cells," Anaesth. Intensive Care Med. **20**, 170–174 (2019).
[33]S. Suresh, "Biomechanics and biophysics of cancer cells," Acta Biomater. **3**, 413–438 (2007).
[34]G. R. Cokelet and H. L. Goldsmith, "Decreased hydrodynamic resistance in the two-phase flow of blood through small vertical tubes at low flow rates," Circ. Res. **68**, 1–17 (1991).
[35]H. L. Goldsmith, G. R. Cokelet, and P. Gaehtgens, "Robin Fahraeus: Evolution of his concepts in cardiovascular physiology," Am. J. Physiol.: Heart Circ. Physiol. **257**, H1005–H1015 (1989).
[36]X. Grandchamp, G. Coupier, A. Srivastav, C. Minetti, and T. Podgorski, "Lift and down-gradient shear-induced diffusion in red blood cell suspensions," Phys. Rev. Lett. **110**, 108101 (2013).
[37]R. K. Singh, X. Li, and K. Sarkar, "Lateral migration of a capsule in plane shear near a wall," J. Fluid Mech. **739**, 421–443 (2014).
[38]D. Leighton and A. Acrivos, "Measurement of shear-induced self-diffusion in concentrated suspensions of spheres," J. Fluid Mech. **177**, 109–131 (1987).
[39]A. Kumar and M. D. Graham, "Mechanism of margination in confined flows of blood and other multicomponent suspensions," Phys. Rev. Lett. **109**, 108102 (2012).
[40]S. Kim, R. L. Kong, A. S. Popel, M. Intaglietta, and P. C. Johnson, "Temporal and spatial variations of cell-free layer width in arterioles," Am. J. Physiol.: Heart Circ. Physiol. **293**, H1526–H1535 (2007).
[41]E. H. Bloch, "A quantitative study of the hemodynamics in the living microvascular system," Am. J. Anat. **110**, 125–153 (1962).
[42]A. Copley and P. Staple, "Haemorheological studies on the plasmatic zone in the microcirculation of the cheek pouch of Chinese and Syrian hamsters," Biorheology **1**, 3–14 (1962).
[43]M. Soutani, Y. Suzuki, N. Tateishi, and N. Maeda, "Quantitative evaluation of flow dynamics of erythrocytes in microvessels: Influence of erythrocyte aggregation," Am. J. Physiol.: Heart Circ. Physiol. **268**, H1959–H1965 (1995).
[44]N. Tateishi, Y. Suzuki, M. Soutani, and N. Maeda, "Flow dynamics of erythrocytes in microvessels of isolated rabbit mesentery: Cell-free layer and flow resistance," J. Biomech. **27**, 1119–1125 (1994).
[45]D. A. Fedosov, B. Caswell, A. S. Popel, and G. E. Karniadakis, "Blood flow and cell-free layer in microvessels," Microcirculation **17**, 615–628 (2010).
[46]M. M. N. Hossain, N. W. Hu, A. Kazempour, W. L. Murfee, and P. Balogh, "Hemodynamic characteristics of a tortuous microvessel using high-fidelity red blood cell resolved simulations," Microcirculation (published online) (2024).
[47]R. E. Bruehl, T. A. Springer, and D. F. Bainton, "Quantitation of L-selectin distribution on human leukocyte microvilli by immunogold labeling and electron microscopy," J. Histochem. Cytochem. **44**, 835–844 (1996).
[48]P. Bongrand and G. Bell, *Cell Surface Dynamics: Concepts and Models* (Marcel Dekker, New York, 1984), pp. 459–493.
[49]D. A. Hammer and S. M. Apte, "Simulation of cell rolling and adhesion on surfaces in shear flow: General results and analysis of selectin-mediated neutrophil adhesion," Biophys. J. **63**, 35–57 (1992).
[50]D. A. Fedosov, J. Fornleitner, and G. Gompper, "Margination of white blood cells in microcapillary flow," Phys. Rev. Lett. **108**, 028104 (2012).
[51]K. B. Abbitt and G. B. Nash, "Rheological properties of the blood influencing selectin-mediated adhesion of flowing leukocytes," Am. J. Physiol.: Heart Circ. Physiol. **285**, H229–H240 (2003).
[52]P. Balogh and P. Bagchi, "A computational approach to modeling cellular-scale blood flow in complex geometry," J. Comput. Phys. **334**, 280–307 (2017).
[53]P. Balogh and P. Bagchi, "Direct numerical simulation of cellular-scale blood flow in 3D microvascular networks," Biophys. J. **113**, 2815–2826 (2017).
[54]P. Balogh and P. Bagchi, "Analysis of red blood cell partitioning at bifurcations in simulated microvascular networks," Phys. Fluids **30**, 051902 (2018).
[55]P. Balogh and P. Bagchi, "Three-dimensional distribution of wall shear stress and its gradient in red cell-resolved computational modeling of blood flow in in vivo-like microvascular networks," Physiol. Rep. **7**, e14067 (2019).
[56]J. Happel and H. Brenner, *Low Reynolds Number Hydrodynamics: With Special Applications to Particulate Media* (Springer Science & Business Media, 2012), Vol. 1.
[57]S. Chien, R. King, R. Skalak, S. Usami, and A. Copley, "Viscoelastic properties of human blood and red cell suspensions," Biorheology **12**, 341–346 (1975).
[58]Y.-C. Fung, *Biomechanics: Circulation* (Springer Science & Business Media, 2013).
[59]G. Tryggvason *et al.*, "A front-tracking method for the computations of multiphase flow," J. Comput. Phys. **169**, 708–759 (2001).
[60]P. Canham and A. C. Burton, "Distribution of size and shape in populations of normal human red cells," Circ. Res. **22**, 405–422 (1968).

[61]S. Chien *et al.*, "Rheology of leukocytes," Ann. N. Y. Acad. Sci. **516**, 333–347 (1987).
[62]R. Skalak, A. Tozeren, R. Zarda, and S. Chien, "Strain energy function of red blood cell membranes," Biophys. J. **13**, 245–264 (1973).
[63]C. Loop, "Smooth subdivision surfaces based on triangles," M.S. thesis (University of Utah, 1987).
[64]F. Cirak, M. Ortiz, and P. Schröder, "Subdivision surfaces: A new paradigm for thin-shell finite-element analysis," Int. J. Numer. Methods Eng. **47**, 2039–2072 (2000).
[65]J. Walter, A. V. Salsac, D. Barthès-Biesel, and P. Le Tallec, "Coupling of finite element and boundary integral methods for a capsule in a Stokes flow," Numer. Methods Eng. **83**, 829–850 (2010).
[66]P. E. Balogh, "The development and application of a computational method for modeling cellular-scale blood flow in complex geometry," Ph.D. thesis (Rutgers The State University of New Jersey, 2018).
[67]M. M. N. Hossain *et al.*, "Angiogenic microvascular wall shear stress patterns revealed through three-dimensional red blood cell resolved modeling," Function **4**, zqad046 (2023).
[68]Parametric Technology Corporation, *PTC Creo Version 8.0* (Parametric Technology Corporation, 2021).
[69]C. Geuzaine and J. F. Remacle, "Gmsh: A 3-D finite element mesh generator with built-in pre-and post-processing facilities," Numer. Methods Eng. **79**, 1309–1331 (2009).
[70]K. Lykov, Y. Nematbakhsh, M. Shang, C. T. Lim, and I. V. Pivkin, "Probing eukaryotic cell mechanics via mesoscopic simulations," PLoS Comput. Biol. **13**, e1005726 (2017).
[71]L. Yang *et al.*, "Modeling cellular deformations using the level set formalism," BMC Syst. Biol. **2**, 1–16 (2008).
[72]X. Wang *et al.*, "Mechanical stability of the cell nucleus–roles played by the cytoskeleton in nuclear deformation and strain recovery," J. Cell Sci. **131**, jcs209627 (2018).
[73]E. H. Barriga and R. Mayor, *Seminars in Cell & Developmental Biology* (Elsevier, 2019), Vol. 93, pp. 55–68.
[74]O. Chaudhuri, J. Cooper-White, P. A. Janmey, D. J. Mooney, and V. B. Shenoy, "Effects of extracellular matrix viscoelasticity on cellular behaviour," Nature **584**, 535–546 (2020).
[75]T. J. Boerner, S. Deems, T. R. Furlani, S. L. Knuth, and J. Towns, paper presented at the Practice and Experience in Advanced Research Computing, Portland, OR, USA, 2023.